

Multi-scale fully convolutional neural networks for histopathology image segmentation: from nuclear aberrations to the global tissue architecture

Rüdiger Schmitz^{a,b,c,*}, Frederic Madesta^{b,c}, Maximilian Nielsen^{b,c}, Jenny Krause^d, René Werner^{b,c,**}, Thomas Rösch^{a,**}

^aDepartment for Interdisciplinary Endoscopy, University Medical Center Hamburg-Eppendorf,

^bDAISYlabs, Forschungszentrum Medizintechnik Hamburg,

^cDepartment of Computational Neuroscience, University Medical Center Hamburg-Eppendorf,

^dI. Department of Internal Medicine, University Medical Center Hamburg-Eppendorf, Hamburg, Germany

Abstract

Histopathologic diagnosis relies on integration of simultaneous information from a broad range of scales, ranging from nuclear aberrations ($\approx \mathcal{O}(0.1\mu\text{m})$) through cellular structures ($\approx \mathcal{O}(10\mu\text{m})$) to the global tissue architecture ($\gtrsim \mathcal{O}(1\text{mm})$).

To explicitly mimic how human pathologists combine multi-scale information, we introduce a family of multi-encoder fully-convolutional neural networks with deep fusion. We present a simple block for merging model paths with differing spatial scales in a spatial relationship-preserving fashion, which can readily be included in standard encoder-decoder networks and at various levels. Additionally, a context classification gate block is suggested as an alternative for the incorporation of solely global context. Furthermore, deep guidance by an additional classification loss is studied.

Our experiments on whole-slide images of hepatocellular carcinoma show that the multi-scale architectures outperform a baseline U-Net by a large margin. The setups benefit from both local as well as global context and particularly from a combination of both. If feature maps from different scales are fused, doing so in a spatial relationship preserving manner is found to be beneficial. Deep guidance seems to speed up and stabilize model training. Additional path fusions are shown to be possible at low computational cost which considerably increases the set of possible multi-scale architectures.

The findings demonstrate the potential of the introduced family of human-inspired, end-to-end trainable, multi-scale multi-encoder fully-convolutional neural networks to improve deep histopathologic diagnosis by extensive integration of largely different spatial scales.

Keywords: Multi-scale, Computational Pathology, Histopathology, Fully-convolutional neural nets, FCN, Human-inspired computer vision

1. Introduction

1.1. Clinical relevance and motivation

If the rumor is tumor, the issue is tissue. Histopathology is the gold standard and backbone of cancer diagnosis, providing important information for various stages of the treatment process

(Brierley et al.). For instance, a fine-grained grading and staging of dysplasia and malignancy in precursor and cancer lesions, respectively, underlies individualized treatment planning in many entities. Moreover, in virtually any operationally curative situation, the assessment of whether the resection specimen margins are free of tumour cells is of vital importance and a core task for clinical pathology.

Human pathologists meet these challenges with the help of elaborated diagnostic criteria and grading systems for all kinds of cancer and cancer precursors. Even though their specific details vary for different kinds of cancer, many rely on a combina-

*Corresponding author: r.schmitz@uke.de.

**Equal contribution.

Abbreviations: *Arch.* – architecture, *CI* – confidence interval, *Clss.* – classification, *FCN* – fully-convolutional neural net, *HCC* – hepatocellular carcinoma, *ms* – multi-scale, *msM* – multi-scale merge-block. *WSI* – whole-slide image.

tion of features such as

- Nuclear inner density, i.e. color, (Zink et al. (2004)) and
- Deformed and varying nuclear shapes or global alterations of the nuclei (Zink et al. (2004)).
- Increased nucleus to stroma ratio and
- Loss of nuclear polarity (e.g. nucleus not at the bottom anymore), as observed in many glandular tumours.
- Deformed cellular shapes and heterogenous cell sizes,
- Loss of organ- and function-defining positions on small (e.g. neighboring cells not in a single layer but some stacked over each other) and larger scales (e.g. atypical or deformed glandular shapes),
- Invasion (i.e. disrespecting global tissue order and borders between different layers)

As can be seen from this (in-extensive) list, diagnosis and grading of malignancy inherently involves a range of different scales. These scales span a factor of about or more than a thousand, ranging from sub-nuclear features (which lie on a spatial scale of $\approx \mathcal{O}(0.1 \mu\text{m})$) over nuclear, cellular ($\approx \mathcal{O}(10 \mu\text{m})$), inter-cellular ($\approx \mathcal{O}(100 \mu\text{m})$) to glandular and other higher organisational features ($\gtrsim \mathcal{O}(1 \text{mm})$).

The importance of the integration of information from different scales is reflected in how human pathologists approach these tasks: Regions of interest are repeatedly viewed at several different magnifications by turning the objective revolver of the microscopy back and forth again and again.

In this work, we aim to develop a family of deep learning models that architecturally mimic this behaviour and examine their potential.

1.2. Related works

With its success in various computer vision tasks, deep learning methods have opened up a myriad of perspectives for computer vision and computer-aided diagnoses (CADx) in histopathology (Litjens et al. (2017)). Image segmentation is a standard task in computer vision and machine learning and can have direct clinical use in the field of pathology: be it the analysis of margin status (i.e. distance of tumor cells to resection margin) or area-dependent grading systems (e.g. Gleason score in

prostate cancer (Epstein et al. (2016))) or special (research) applications that require morphological analysis of multiple tissue sections (Schmitz et al. (2018); Segovia-Miranda et al. (2019)).

In medical image analysis, fully convolutional neural networks (FCNs, Long et al. (2015)) and, most prominently, U-Net-based architectures (Ronneberger et al. (2015)) have successfully been adopted to segmentation tasks in a plenty of different scenarios imaging modalities (Litjens et al. (2017); Isensee et al. (2018)). The same holds for the field of computational histopathology (Bulten et al. (2019); Liu et al.; Campanella et al. (2019)). In many of these works, generic computer vision networks, mainly standard U-Nets, have indeed successfully been applied to histopathology images. Beyond that, there are some approaches for specialized histopathology architectures (Bejnordi et al. (2017); Li et al. (2017); Vu and Kwak (2019)) and training techniques (Campanella et al. (2019); Wang et al. (2019)). Some of these works touch upon the question on how additional context can be provided to the network. However, the strategies that have been proposed hitherto are mainly confined to local, same-scale context (Bejnordi et al. (2017); Li et al. (2017)) and/or sliding-window CNN techniques (Bejnordi et al. (2017)). For 3d medical images, Kamnitsas et al. (2017) have proposed the use of multiple paths operating at different but similar spatial scales in order to alleviate the problem of an otherwise very limited patch size in memory-costly 3d-nets.

Also beyond the medical image domain, introduction of image context has been a topic of interest. Early studies in natural image processing have leveraged contextual information by global pooling of feature maps that are then unpooled and concatenated to the original feature maps (Liu et al. (2015)). More modern approaches aim at an increase of the receptive fields through dilated or atrous convolutions and atrous spatial pyramid pooling (Chen et al. (2017a,b)) which have turned out to be powerful techniques for inclusion of same- or similar-scale context. Alternatively, Zhang et al. (2018) let the FCN explicitly predict "scaling factors" for the possible classes from its bottle-neck layer, which are then used to multiply and thus "highlight" the respective feature maps at the final layer. The "scaling factors" can capture the overall image content and can thus be learned through use of an additional classification loss. Recently, Zhou et al. (2019) have, again using atrous convolutions,

proposed the use of a reinforcement-based strategy involving two sub-nets, one for encoding context and one for the actual segmentation task.

By the properties of the natural images under consideration in these studies, namely the limited image size as compared to histopathologic whole-slide images (WSIs), the scales of detailed and contextual features are much less different than in our problem. Congruously, the common aim of the above approaches has rather been to "help clarify local confusion", (Liu et al. (2015)), or to make better use of what is inputted to the net anyways, rather than introduction of otherwise unavailable information from much different scales as in our case. In short, context as a topic of research in natural image computer vision, mainly means optimized use of information that (mostly) is available to the network. Context as we understand it in the present paper, however, rather refers to the introduction of information that is otherwise entirely unavailable to the network, namely features from much larger scales.

1.3. Contributions

There exists a plenty of highly optimized, U-Net derived architectures including, for instance, elaborate skip connections (Badrinarayanan et al., 2017), dense connections (Li et al., 2018), attention gating techniques (Oktay et al., 2018) and newer FCN architectures like DeepLab (Chen et al., 2017a). Nevertheless, standard U-Nets have turned out to be robust work horses for many medical computer vision tasks and are hard to beat by internal modifications of the base architecture (Isensee et al. (2018, 2019)). However, histopathology diagnosis is, by the nature of the large whole-slide images and the with multiple features from very different scales closely interwoven, a very specific task.

Therefore, this work shall, drawing on a standard base model, explore whether the architectural mimicry of how human experts approach this specific task can improve fully-convolutional neural networks for histopathology image segmentation.

Consequently, the main contributions of this paper are as follows: We introduce a family of U-Net-based fully convolutional deep neural nets that are specifically designed for the extensive integration of largely different spatial scales. First, we propose a simple building block that can fuse various encoders with different spatial scales in a manner that preserves the relative spatial scales. As a light-weight alternative, we also propose the use of an

independent context classification model for gating the segmentation model output. Second, we use these building blocks for the construction of different multi-scale FCNs and show that these outperform a baseline U-Net architecture. Third, by a systematic, stepwise analysis, we identify relevant spatial scales, examine the necessity of preserving spatial relationships between different encoders, investigate possible benefits from deep guidance by an additional classification loss and study the effects of multiple path fusions. Based on this, we narrow down the possible multi-scale setups and comment on how to systematically adapt the presented multi-scale FCN family to specific tasks in histopathology deep learning.

2. Materials & methods

2.1. Dataset

Experiments in this study are conducted using the public dataset provided for the PAIP 2019 challenge (part of the MICCAI 2019 Grand Challenge for Pathology Choi et al.). It is comprised of 50 de-identified whole-slide histopathology images from 50 patients that underwent resection for hepatocellular carcinoma (HCC) in three Korean hospitals (SNUH, SNUBH, SMG-SNU BMC) from 2005 to June 2018. The slides have been stained by hematoxylin and eosin and digitalised using an Aperio AT2 whole-slide scanner at $\times 20$ power.

Regions of viable cancer cells as well as the whole cancer regions (additionally including stroma cells and so forth) have manually been annotated as described in (Choi et al.). Figure 1 shows an exemplary whole-slide image from the dataset. It is worth noting that all individual cases of the given dataset do indeed include cancer regions.

All de-identified pathology images and annotations used in this research were prepared and provided by the Seoul National University Hospital under a grant from the Korea Health Technology R&D Project through the Korea Health Industry Development Institute (KHIDI), funded by the Ministry of Health & Welfare, Republic of Korea (grant number: HI18C0316).

This dataset is ideally suited for our study for the following two reasons: First, it is, to our knowledge, the first publicly available dataset for histopathology image segmentation that is composed of full-size whole slide images (WSI) rather than image crops of some hundred to few thousand pixels per

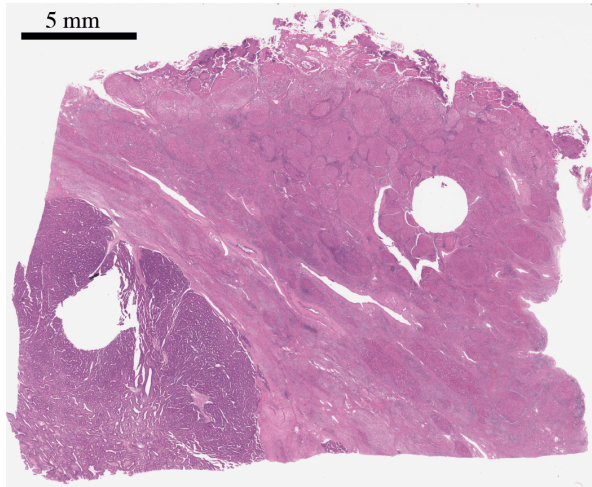


Figure 1: An exemplary case from the PAIP dataset. The tissue sample is stained by hematoxylin and eosin. A hepatocellular carcinoma (HCC) can be identified in the bottom left corner of the image. The so-called "pseudocapsule" around it is a typical, though not obligatory, feature of HCC. Scanned with a resolution of some $0.1\mu\text{m}$ per pixel (this dataset: $0.5021\mu\text{m}/\text{px}$), the width and height of a typical whole-slide image of this kind are on the order of some ten thousand pixels each, resulting in a gigapixel-sized image.

axis. Second, hepatocellular carcinoma is a prominent example of a cancer that has specific signs on different spatial scales, namely nuclear aberrations, local tissue abnormalitis and large-scale features such as a so-called "psuedocapsule".

2.2. Preprocessing

As compared to the annotations originally provided for the PAIP challenge, which comprise the classes "viable tumour" and "whole tumour" (i.e. including viable tumour cells, stroma, necrosis, ...), we added "overall tissue" as an another class for improved patch balancing and as a target for stain normalization. The "annotations" for the "overall tissue" class are created fully automatically before training, namely by thresholding of the original images with $[R, G, B] \leq [235, 210, 235]$ and subsequent application of morphological opening and closing operations. This threshold is the same as the one that has been used by the challenge organisers for cleaning of the whole and viable tumour annotations.

Images are standardised by Reinhard colour normalisation (Reinhard et al. (2001)) with respect to the "overall tissue" regions and normalised to channel-wise zero average and unit variance.

2.3. Model training

For our experiments, we aim at reproducing a standard and widely used setup as much as possible. This includes use of a common model as the base line (see below), as well as the remainder of the training conditions and hyperparameters. The training strategy and all hyperparameters have manually been optimized for training of the baseline Res18-Unet before the experiments and then kept fixed for all models and throughout all experiments.

The training process is split into (short pseudo-)epochs of 1920 patches each, with all patches randomly redrawn after each individual "epoch". This allows for a close inspection of the training process, and, as compared to the use of a fixed number of pre-selected patches, it reduces overfitting given the limited memory resources and the enormously large whole-slide images. All models are trained for at least 120 pseudo-epochs (230,400 iterations) or until convergence of the validation loss was reached.

For each pseudo-epoch, the patches are balanced with respect to both the individual cases in the training set and the available classes (background, overall tissue, whole tumour, viable tumour). Our models are implemented using PyTorch (Paszke et al. (2017)). Training is conducted by use of an in-house developed training pipeline for generic multi-modal medical image deep learning. Optimisation is performed using Adam (Kingma and Ba (2014)) employing a learning rate of 10^{-3} and a learning rate decay with $\gamma = 0.5$ every 30 epochs (57,600 iterations). During training, we employ online data augmentation including the following standard operations: rotation, flip along the horizontal axis, saturation and brightness transformation.

We choose the binary cross entropy (BCE) loss as a common and widely used loss function for this study. In order to balance for class inhomogeneities and draw attention to the tumour regions, we use class-weights of $[0, 1, 2, 6]$ for background, overall tissue, whole tumour and viable tumour, respectively. BCE is used as a loss function for both classification (if the model has an additional classification output, cf. section 3.2) and segmentation.

2.4. Validation strategy & statistical analysis

We use a 5-fold cross validation (CV) strategy with the split conducted at the level of entire WSIs (one WSI corresponding to one case). The primary outcome parameter of the study is the class-averaged Jaccard index at model convergence. The

best class-averaged Jaccard index as well as the viable tumor Jaccard index and the number of iterations until convergence are recorded separately.

For all models and splits, validation is conducted after the following epochs (number of iterations): 1 (1,920), 3 (5,760), 5 (9,600), 8 (15,360), 11 (21,120), 16 (30,720), 21 (40,320), and then every 10 epochs (19,200 iterations). At each validation step, four 3072×3072 px-sized sub-images per image are evaluated (totalling 40 sub-images from 10 images per split). The positions of these sub-images are randomly chosen with the condition that for any WSI all four classes shall be represented in at least one of its sub-images. Sampling of the sub-image positions is done once, before the first experiment, and then kept fixed throughout all experiments. This means that all models for a given split are evaluated with respect to exactly the same sub-images at all validation steps.

2.5. Statistical analysis

For a given model, performance scores are reported per split, plus the mean and 95%-confidence interval (CI) across the five splits. In order to set a robust baseline, all experiments for the baseline model are repeated three times and the mean values are reported in section 5.1, corresponding to a conservative estimate (over clustered experiments). The results for the individual runs of the baseline model are provided in the Supplementary Materials.

For the analysis of statistical significance, results obtained for different models but corresponding CV splits are considered as paired measurements. Use of a paired-sample t-test, however, requires statistical independence of the experiments which is violated in a cross-validation setting. Therefore, we perform a corrected resampled paired-sample t-test, with the (conservative) correction as introduced by (Nadeau and Bengio (2000)) and discussed by (Bouckaert and Frank (2004)). For the reason that all multi-scale architectures can reproduce the behaviour of the baseline U-Net, we use a one-sided resampled paired-sample t-test. Additionally, in order to correct for multiple testing, we employ the Benjamini-Hochberg step-up procedure.

Using the results from the baseline model alone (cf. section S2), we seek to pre-estimate the statistical power of our study: We estimate the standard deviation of the Jaccard index for a single model to be in the range of 0.045. Therefore, for the standard deviation of the differences between two mod-

els, we assume $\sqrt{2} \cdot 0.045$. The resampling correction by Nadeau and Bengio can be viewed as an additional factor of $\left(\frac{1}{n} + \frac{n_{val}}{n_{train}}\right) / \sqrt{\frac{1}{n}}$ to the otherwise under-estimated standard deviation, where n denotes the number of CV splits and n_{train} and n_{val} are the number of samples in the train and validation set, respectively. In our case, with $n_{train} = 40$ and $n_{val} = 10$, this computes to 1.5. Therefore, we can estimate the power of our study to be equal to the power of a standard paired-sample t-test with a standard deviation of the pairs of $1.5 \cdot \sqrt{2} \cdot 0.045$. We aim for an improvement over the baseline U-Net of 0.1 to 0.15 for the multi-scale models, resulting in a statistical power in between 0.613 and 0.888, which we regard as acceptable. For differences between different multi-scale models, which we expect to be around 0.05, however, our study is clearly underpowered (statistical power 0.253). We therefore conclude that comparisons of multi-scale architectures with respect to the baseline U-Net are amenable to an analysis of statistical significance, whereas differences within the family of multi-scale models are not.

All statistical analyses were performed using R 4.0.0 (R Core Team (2013)).

2.6. Baseline method

Beyond the still popular sliding-window CNN-based techniques, U-Net-based FCN architectures form the de facto standard in the medical image domain (Isensee et al. (2018)), including histopathology (Litjens et al. (2017)). Beating the standard U-net by internal modifications is evidently hard (Isensee et al. (2019, 2018)) and beyond the scope of this work. Rather, as outlined in the introduction, this study shall examine whether by designing a model of standard components but with its larger architecture mimicking human expert diagnostic procedures, further improvement can be made.

Therefore, we choose a non-modified ResNet18-based U-Net (He et al. (2015)) being a common, standard U-Net variant as the baseline for this study. An implementation of this architecture can be found in ¹. For a detailed description of the model, the reader may be referred to section S2 in the Supplementary Materials. In brief, the

¹<https://github.com/usuyama/pytorch-unet>. Accessed:2019-09-19.

ResNet18 forms the encoder of the otherwise standard U-Net architecture (cf. figure S1). The encoding ResNet18 has been pre-trained on the ImageNet dataset (Russakovsky et al. (2015)). For our study, the baseline model is trained at full-resolution patches of the size 512×512 .

3. Multi-scale multi-encoder models

In order to provide the network with local architectural information (cf. figure 2 and the considerations in section 1), we construct a family of multi-scale multi-encoder networks building upon the baseline Res-U-Net architecture.

Technically, it is worth noting that whole-slide images (WSI) are commonly saved as so-called pyramid representations which contain the original image in multiple scales ("downsample levels"). Such representations underlie the common WSI formats such as *.mrxs, *.czi, *.svs and others. Therefore, when working with WSI images, multiple scales can directly be loaded from file and, even with very broad context, come with a moderate overhead only.

In the following, we first introduce the underlying blocks that we use for integration of multi-scale context, namely the *multi-scale merge block* and the *context classification gate*. Afterwards, we describe the different variants of our setup that shall be examined in this study. The source codes of the models described herein are publicly available at ².

3.1. Multi-scale merge block: spatial relationship preserving path fusion in multi-scale multi-encoder models

Figure 3a sketches the functioning of the multi-scale merge block. At the bottleneck level, the feature maps from both the main encoder and the side (context) encoder have sizes of $16 \times 16 \times 512$. In order to spatially match the output of the full resolution encoder, a $n' \times n'$ center cropping ($\mathcal{S}_{\frac{16}{n'} \times \frac{16}{n'}}$) of the n -times down-scaled context path is performed followed by $n \times n$ bilinear upsampling ($\mathcal{U}_{n \times n}$), where $n' = 4$ if $n = 4$ and $n' = 8$ if $n = 16$. For the case $n' \neq n$, another center cropping with 16×16 is conducted. Both, now spatially consistent, paths are then merged by concatenation. Finally, the number

of feature maps is reduced to the original number by a 1×1 convolution. This operation shall learn which of the feature maps from the two paths are relevant and how they need to be related to each other.

For application to multiple context encoders, spatial alignment is ensured for any individual context encoder in the same manner as described above. The spatially-aligned feature maps from all encoders are then concatenated. Afterwards, the feature map size is reduced by a 1×1 convolution with $512 \cdot (m + 1)$ input feature maps and 512 output feature maps, $c_{1 \times 1}^{512 \cdot (m+1), 512}$, where m denotes the number of side encoders.

3.2. Context classification gate

One can try to predict the (probable) contents of the central detail patch by solely looking at the global context patch (cf. figure 2). As multiple, even mutually exclusive, classes can be included in the detail patch, this states a multi-label classification problem. Alternatively to integration of multi-scale context to earlier layers of the base network (by use of multi-scale merge blocks), this information of the probable contents of the detail patch can be passed to the segmentation network right at the end of the decoder, i.e. just before the final activation, in order to "gate" the probability maps for the segmentation by the probabilities that, judging by the global context, the respective class is present anywhere, at all.

This idea underlies the context classification gate depicted in figure 3b. The classification net outputs a probability value for each individual class (illustrated by the colored boxes in the bottom left corner). These are multiplied to the probability maps of the segmentation network in a channel-wise manner (as in excitations in squeeze-and-excite blocks, cf. (He et al., 2015)), thereby emphasizing probable classes and suppressing unlikely diagnoses. To allow the segmentation network to either use this information or break this guidance, a "leak" is constructed by concatenation of the original, unexcited feature maps to the excited ones, followed by a 1×1 convolution that is to learn how to combine the excited and the leaked feature maps.

3.3. msY-Net: Integrating context and tissue architecture

The msY-Net is provided with two input patches of the scales 1 and 4 (which correspond to the inner

²<https://github.com/RSchmitzHH/multiscale>. Please do not hesitate to contact the corresponding author for help with implementation and usage.

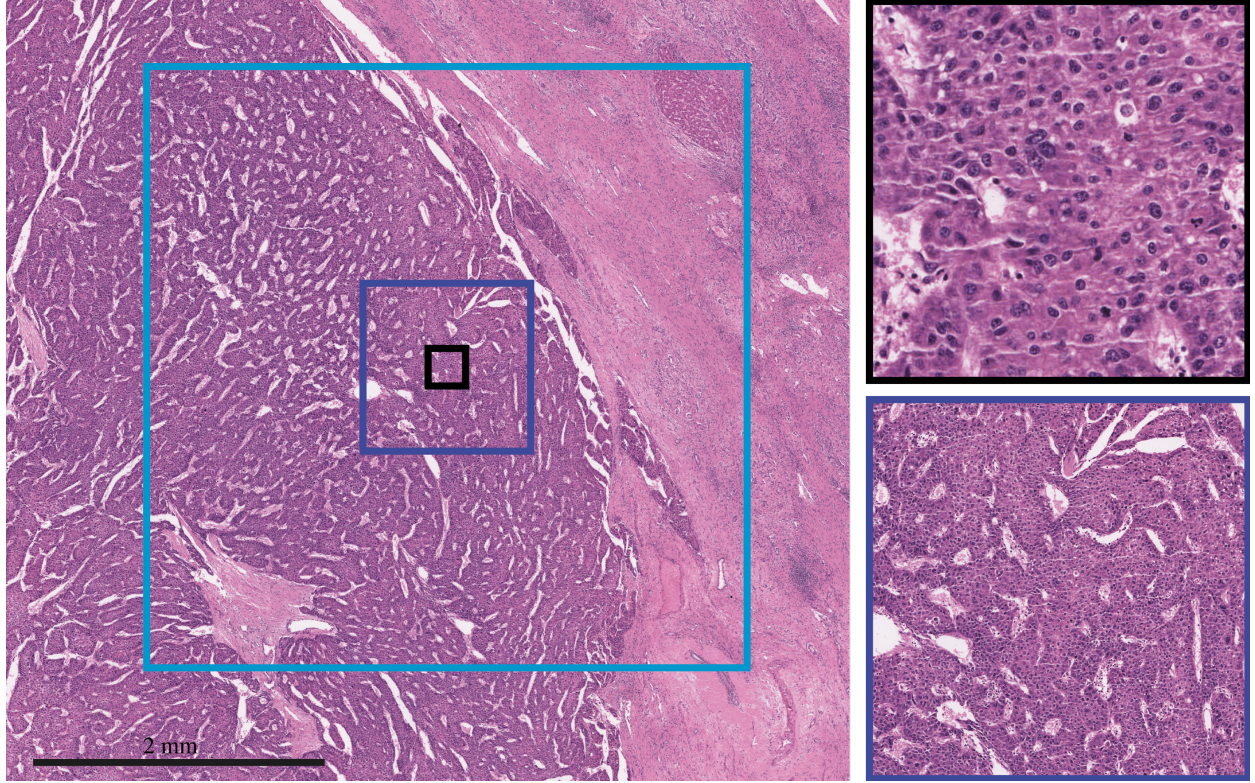


Figure 2: Input patches to the different models under consideration, shown in an illustrative region of the same whole-slide image as depicted in figure 1. The innermost, black rectangle corresponds to a 512×512 patch of the scale 1 which we refer to as the "detail patch". (The top right inset provides a zoomed view of the detail patch.) The next, dark blue rectangle corresponds to a 572×572 patch of the scale 4. As can be seen, it contains information on how the cells are organised in strands and "trabeculae" (or whether the cells violate these patterns). These information are hard or impossible to deduce using the innermost patch alone. In this sense, it adds "architectural" information. We refer to it as "local context" or the "local context patch". (A zoomed view of it is shown in the bottom right inset.) The outermost, light blue rectangle, which we call a "global context patch", contains information on the large-scale organisation of the tissue, such as the pseudocapsule, for instance, that is typical for hepatocellular carcinoma. Whilst a standard U-Net is provided with the information from the detail patch solely, a msY-Net architecture (section 3.3) can integrate information from the detail patch plus either the local or the global context patch. The msY²- and msYI-Net architectures are two options for integration of all three scales. The scale bar is 2 mm.

two rectangles in figure 2) or 1 and 16 (inner and outer rectangle) as an input. The full-resolution patch (scale 1) is fed into the standard U-Net architecture. The other is passed through a separate but analogous encoder architecture ("context encoder") built from another ResNet18. As the skip connections in the U-Net are for helping the decoder re-localise the high-level features and only the full-resolution patch is the one that needs to be segmented, the context encoder does *not* have any skip connections to the decoder.

The two paths are merged at the bottleneck of the original U-Net by use of the spatial relationship preserving multi-scale merge block (cf. section 3.1). The resulting overall architecture is sketched

in figure 4b.

In the following, we refer to a msY-Net that uses detail patches of the scale 1 and context patches of the scale n as msY_(n).

3.4. msYI-Net and msY²-Net: Integration of global and local context

In order to provide the model with large- and small-scale context information at the same time, we construct two models that have two context encoders for the scales 4 and 16.

We examine two different ways of how to add this information to the underlying msY-Net: First, we add both context encoders in the same way as the first context-encoder of the msY-Net has

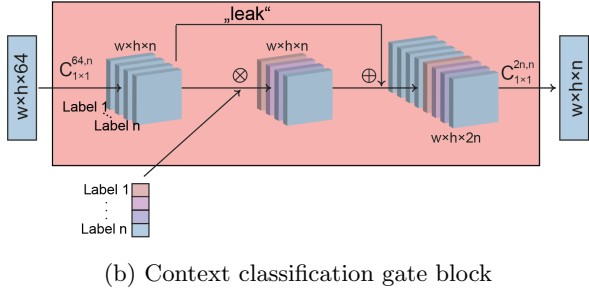
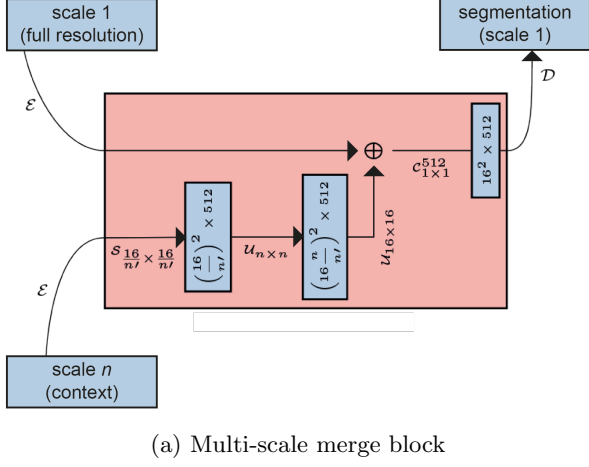


Figure 3: Schematic illustration of the multi-scale merge block (a) and the context classification gate block (b). \mathcal{E} , \mathcal{D} are the encoder and decoder path of the network (cf. figure 4b), respectively. The blue upward boxes are the feature maps with their respective sizes printed inside. \oplus shall denote concatenation and \otimes channel-wise multiplication. The "leak" connection is a copy followed by concatenation. $\mathcal{S}_{x \times y}$ stands for the central cropping of the size $x \times y$ in the spatial dimensions and $\mathcal{U}_{a \times b}$ the bilinear upsampling by factors of a and b in the dimensions 1 and 2. w and h denote the spatial width and height, n the number of classes. $\downarrow_{n_1, n_2}^{a, b}$ means the $n_1 \times n_2$ convolution with a input feature maps and b output features maps, where a may omitted if the size of its input is explicitly given, followed by ReLU activation.

been added before, i.e. through another multi-scale merge block following the first multi-scale merge block. We refer to this model as msY²-Net. We explore two different variants of the msY²-Net: one with an additional classification output from the global context path (cf. figure 4c) and one without it.

For the second variant, we keep the large-context encoder separate, *parallel*, so to say, to the underlying msY-Net. This model is outlined in figure 4e. The *I* in the name msYI-Net shall refer to the large-context encoder paralleling the underlying msY-Net *without* any fusion at the bottleneck or before. Also

the large-context encoder in this model consists of another ResNet18, which is used for classification of the overall content of the full-resolution patch. Hence, the network has two outputs, the segmentation of the full-resolution patch from its msY-Net part and the classification of the full-resolution patch contents from the large-context encoder, its *I*-part. Additionally, the final logits of the two paths are combined by a context-classification gate. This block basically lets the segmentation path adjust its final logits by the logits of the classification path (cf. section 3.2).

In the msY-Net and the msY²-Net architectures, spatial correspondence between the full resolution encoder and the context encoder(s) is enforced in the multi-scale merge block (cf. figure 3). It should be noted that for the large-context encoder in the msYI-Net, there is no such requirement. Therefore, this model can, in principle, be fed with large-context patches of entirely arbitrary scales.

3.5. Classification loss guidance

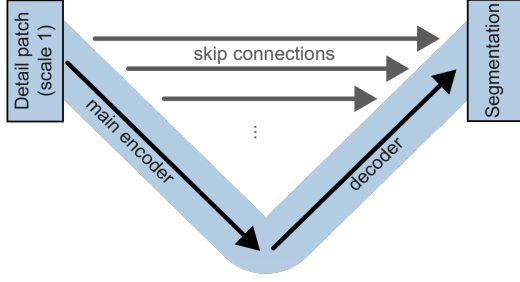
Additional loss functions can improve the training of specific parts of U-Net-based architectures and are used in various manners (Kickingeder et al. (2019); Li and Tso (2019)), including as a classification loss on an additional output derived from the bottleneck feature maps (Mehta et al. (2018)).

Analogously, we compute a classification output from the feature maps of global context encoders (i.e. those with input scale 16) and use it to compute an additional classification loss. The classification loss is computed with respect to the contents of the detail patch. As described in section 2.3, we use a BCE loss for the classification problem and add it to the segmentation loss.

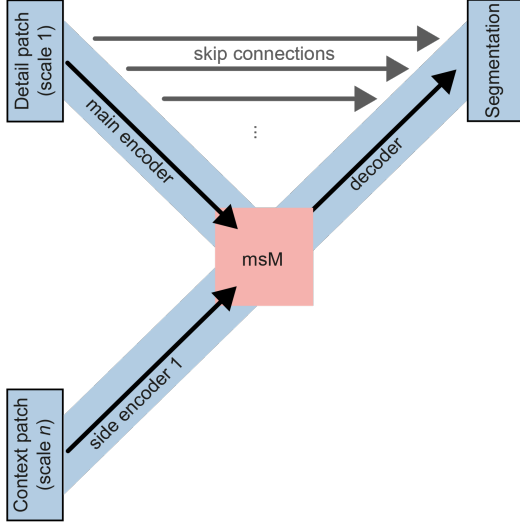
By the additional classification loss, we want to explicitly force the global context encoder, which might otherwise be too weakly related to the small detail patch in its center, to predict the contents of the detail patch from its large-scale context.

3.6. Early and multiple fusions by multi-scale merge blocks

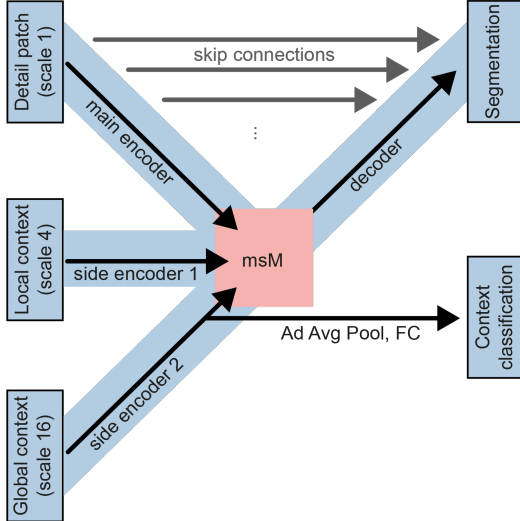
Placement of the multi-scale merge block at the bottleneck level is not obligatory. Technically, a multi-scale merge block can be placed at any level between any two encoders whenever the one shall influence the other (the connection is directed, not mutual). Also, placement of multiple multi-scale merge blocks is possible. Very early merge blocks



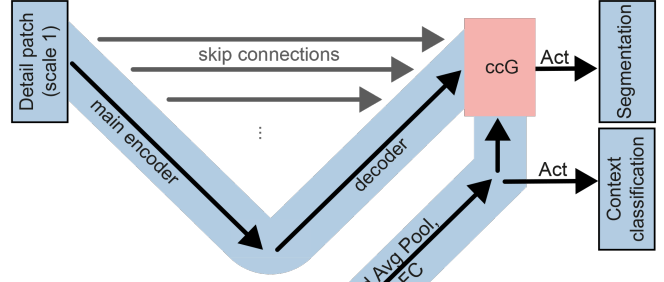
(a) U-Net (baseline)



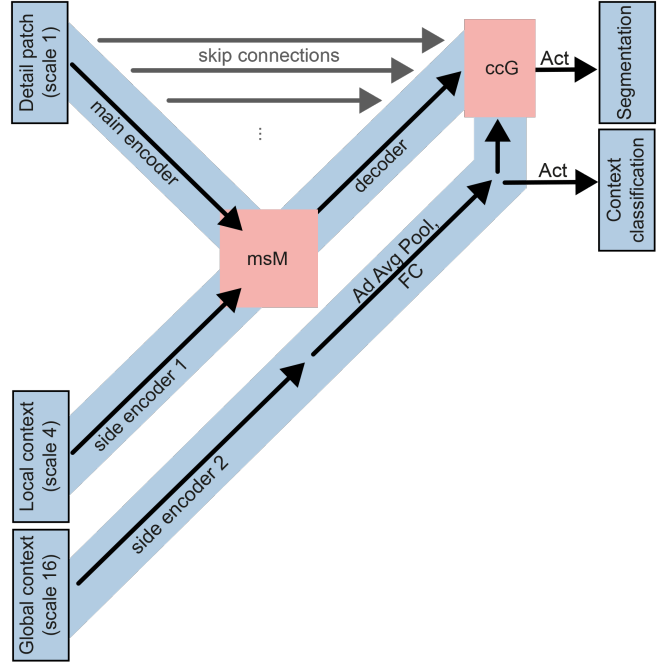
(b) msY-Net



(c) msY²-Net



(d) msUI-Net



(e) msYI-Net

Figure 4: Schematic illustration of the main architectures studied in this paper. All main and side encoders use an (ImageNet-pretrained) ResNet-18. The skip connections and the decoder are the same throughout all of our models (cf. section S1 for details). The multi-scale merge (msM) and context classification gate (ccG) blocks are as described in the sections 3.1 and 3.2 and sketched in figure 3. Ad Avg Pool denotes adaptive average pooling, FC a fully-connected layer and Act the activation function.

will, however, not provide much context due to the still small receptive fields combined with the cropping operation inside the merge block.

On the other hand, earlier and in particular multiple fusions may possibly allow for additional processing of the combined features and, hence, enable modelling of more complex combined features.

It should be noted that this multiple merges are computationally not too costly, as they only introduce additional learnable parameters through the 1×1 convolutions inside the merge blocks.

4. Experiments

We design our experiments as follows: In our first experiment, we examine the basal variants of the multi-scale multi-encoder architecture and compare them to the baseline U-Net. For the additional experiments (4.2 - 4.4), we seek to provide a rationale for these findings and aim narrow down the possible choice of architectures to a smaller set of possible optimal ones.

4.1. Comparison of multi-scale multi-encoder architectures to the baseline U-Net

The primary outcome of this study is whether the proposed multi-scale architectures perform better than the standard U-Net and whether this is a consistent effect.

To this end, for the first experiment, we compare different multi-scale multi-encoder architectures to a baseline U-Net. This results in a total of $N = 6$ pairwise model comparisons. As already described in section 2.5, we correct for the multiple testing using the BenjaminiHochberg step up procedure.

Secondary, we also seek to compare the different multi-scale architectures amongst each other. As our study is underpowered for finding statistically significant results in between different models of the multi-scale family (cf. section 2.5), we do not conduct significance tests for these comparisons but only descriptively present and discuss their results and differences.

4.2. Spatial alignment in multi-scale merge blocks

We hypothesize that spatial matching is a necessary step in the multi-scale merge block. In order to check this hypothesis, we compare the msY²-Net with the multi-scale merge blocks as described above to a msY²-Net variant where the multi-scale

merge blocks are replaced by concatenation followed by a 1×1 convolution. This corresponds to a multi-scale merge block but without alignment of the spatial scales and without preserving spatial relationships. The rest of the spatially non-aligned msY²-Net variant remains unchanged.

If our hypothesis holds and the spatially non-aligned msY²-Net does perform weaker than its standard variant with the correct multi-scale merge block, it will be interesting to examine whether this is "only" due to the clumsy initialization and can potentially be overcome. One might hypothesize that the deficit could be caused by the 1×1 convolution in the merge block being initialized randomly such that the activations from the two context encoders dominate over the main encoder when the signal is passed to the decoder. In order to check whether the supposed deficit from the missing alignment is only due to the introduction of new, untrained convolutions in the middle of the otherwise pretrained encoder, we examine two different variants of the non-aligned model: one variant with randomly initialized weights and another variant where the 1×1 conv is initialized with the unit matrix at the channels belonging to the main encoder and with 0's everywhere else, both superimposed with random noise (normal distribution with standard deviation 10^{-4}). In the latter, the main encoder corresponds to the unperturbed, pretrained model at the beginning of the training process, up to noise.

4.3. Early and multiple merging

Multi-scale merge blocks allow for early and multiple fusions, which may allow for additional processing of combined features. Very early merge blocks, however, do not bring much additional context due to the cropping step inside the multi-scale merge block.

In order to study whether an effect through early and multiple merges can be found in this study, we compare the msY₍₁₆₎-, the msY²- and the msYI-Net to the analogues of them with multi-scale merge blocks on all levels of the encoder.

4.4. Context classification loss

We hypothesize that when using a global-scale encoder, introduction of an additional context classification loss as a means of "guidance" may benefit the model. In order to examine whether this is consistently the case, we create train the following

models with and without context classification loss: $\text{msY}_{(16)}$, msY^2 , $\text{msY}_{(16),MM}$.

5. Results

5.1. Performance improvements through multi-scale multi-encoder setups

The primary outcome of our experiments is whether the proposed multi-scale architectures can achieve an improvement over a baseline U-Net model for histopathological tumor segmentation.

Table 1 reports the average Jaccard index for the two non-trivial classes, viable tumor and whole tumor, at model convergence. Various other performance scores, including for the individual classes, are reported in the Supplementary Materials and show similar results.

The first experiment shows a number of aspects: First and most importantly, there is a considerable improvement over the baseline U-Net by adding multi-scale input. The effect is found to be statistically significant in our experiments, even when tested only for five CV folds and even with a conservative correction for both the multiplicity of the pairwise comparisons and the violation of the independent samples-assumption underlying standard t-statistics.

Concerning the pairwise comparisons between different multi-scale architectures, our data suggest that the global context patch provides more valuable information than the local context patch. The combination of both local and global context might lead to an improvement, as the msY^2 - and the msYI -Net models are consistently found amongst the top performing approaches, but this effect seems marginal and cannot be reliably detected through this study. However, these may be a dataset-specific findings, particularly as it fits the properties of hepatocellular carcinoma (cf. Discussion).

5.2. Necessity for spatial alignment in multi-scale merge blocks

Drawing on theoretical considerations, we have constructed the multi-scale merge blocks such that spatial relationships between the different paths are preserved upon fusion.

Table 2 repeats the results for the msY^2 -Net and compares them two variants of the same architecture which both do *not* adhere to the above condition. These are constructed by just concatenating the bottleneck feature maps from the different

paths without any spatial alignment as part of the multi-scale merge block (cf. section 4.3 for details).

The two variants differ in that the merging 1×1 convolution is either initialized randomly or with pre-defined weights leaving the main path unperturbed at training startup (cf. section 4.3 for details).

It can be seen that both these variants perform consistently weaker than our proposed msY^2 -Net, even though the small sample size precludes statistical significance (corrected resampled t-test $p = 0.057$ and $p = 0.194$, standard t-test $p = 0.017$ and $p = 0.079$).

This is irrespective of whether the weights of the 1×1 convolution are randomly initialized or whether they are initialized such that the ResNet18 encoder of the underlying U-Net is left untouched by the un-aligned merge connections. This fact suggests that the deficit through the missing alignment step may be architectural rather than only a disturbance of the pretrained encoder by the additional 1×1 convolution.

We therefore conclude that, when merging paths at the bottleneck level in a manner as done by the multi-scale merge block, spatial matching is a necessary step.

5.3. Additional merge-connections for early fusion

Table 3 compares the standard msY^2 -, the $\text{msY}_{(16)}$ - and the msYI -Net with multi-scale merge blocks only at the bottleneck to their respective analogues with multi-scale merge connections at every level of the encoder.

Our study cannot find any relevant differences between single-merge and multiple-merge setups. It should be noted, however, that the additional merge connections did at least not lead to any instability in model training.

5.4. Loss-guidance for global context encoders

In order to examine whether the additional classification loss is indeed helpful for “guidance” of the global context encoder, we again examine the msY^2 -, the $\text{msY}_{(16)}$ - and the msYI -Net. Table 4 depicts the resulting class-averaged Jaccard indices for the three models when trained with or without an additional classification loss. In addition, also the number of iterations until convergence (in units of thousands) are shown.

Even though the global context encoder is trained by feedback which originates from the vanishingly

Table 1: Selected multi-scale multi-encoder setups versus the baseline U-Net. The figures in the table depict the class-average of the Jaccard index for whole and viable tumor at validation loss convergence. A \star denotes statistical significance at the level of 0.05. For the other comparisons described in section 5.1, the null hypothesis cannot be rejected at 0.05. For a quick overview, the best results per split and overall are marked bold, ignoring differences < 0.01 .

Arch.	Scales	CV folds					Mean (95% CI)	
		0	1	2	3	4		
U-Net	1	0.766	0.698	0.639	0.704	0.676	0.697 (0.656, 0.737)	
msY-Net	1, 4	0.883	0.752	0.655	0.755	0.709	0.751 (0.677, 0.825)	\star
	1, 16	0.811	0.843	0.724	0.870	0.855	0.820 (0.770, 0.871)	\star
msUI-Net	1, 4	0.782	0.798	0.691	0.851	0.847	0.794 (0.737, 0.851)	
	1, 16	0.833	0.779	0.760	0.883	0.868	0.825 (0.777, 0.872)	\star
msYI-Net	1, 4, 16	0.838	0.840	0.737	0.889	0.880	0.837 (0.784, 0.890)	
msY ² -Net	1, 4, 16	0.861	0.811	0.726	0.897	0.823	0.824 (0.768, 0.880)	

Table 2: Spatial alignment at multi-scale path fusion. Numbers are the class-averaged Jaccard indices at validation loss convergence. All models are variants of the msY² architecture, either with spatial alignment at the multi-scale merge block (1, as per default) or without (2, 3). The best results per split and overall are marked bold.

msY ² -Net variant	CV folds					Mean (95% CI)
	0	1	2	3	4	
spatially aligned ¹	0.861	0.811	0.726	0.897	0.823	0.824 (0.768, 0.880)
non-aligned, init ²	0.851	0.735	0.669	0.810	0.786	0.770 (0.708, 0.832)
non-aligned, random ³	0.809	0.756	0.734	0.759	0.788	0.769 (0.744, 0.795)

Table 3: Multi-level multi-scale merging: For three different multi-scale architectures, the standard variant with multi-scale fusion only at the bottleneck and by a single multi-scale merge block ("bottleneck") is compared to an analogous architecture, but with a multiple multi-scale fusions through one multi-scale merge blocks at each individual encoder level ("multiple"). Numbers are the class-averaged Jaccard indices at validation loss convergence. The best performance per pairwise comparison and split are marked bold, where differences < 0.01 are considered on par.

Arch.	Merge block(s)	CV folds					Mean (95% CI)
		0	1	2	3	4	
msY ² -Net	bottleneck	0.861	0.811	0.726	0.897	0.826	0.824 (0.768, 0.880)
	multiple	0.842	0.839	0.701	0.858	0.816	0.811 (0.755, 0.867)
msY ₍₁₆₎ -Net	bottleneck	0.811	0.843	0.724	0.868	0.855	0.820 (0.770, 0.871)
	multiple	0.814	0.772	0.744	0.887	0.849	0.813 (0.763, 0.863)
msYI-Net	bottleneck	0.838	0.840	0.737	0.889	0.880	0.837 (0.784, 0.890)
	multiple	0.842	0.848	0.745	0.844	0.850	0.826 (0.786, 0.866)

Table 4: Classification loss guidance for the global context encoder. Numbers are the class-averaged Jaccard indices at validation loss convergence, and the number of iterations until convergence in square brackets (in units of 1,000). The best performance (in terms of Jaccard index) per pairwise comparison and split are marked bold, where differences < 0.01 are ignored.

Arch.	Cls. loss	CV folds					Mean (95% CI)
		0	1	2	3	4	
msY ² -Net	with	0.861 [117]	0.811 [174]	0.726 [117]	0.897 [156]	0.826 [156]	0.824 (0.768, 0.880) [116 (range: (116, 156))]
	without	0.854 [252]	0.824 [252]	0.723 [213]	0.804 [175]	0.751 [230]	0.791 (0.744, 0.838) [224 (range: (175, 252))]
msY ₁₆ -Net	with	0.811 [346]	0.843 [156]	0.724 [136]	0.868 [194]	0.855 [538]	0.820 (0.770, 0.871) [274 (range: (136, 538))]
	without	0.856 [365]	0.769 [288]	0.714 [288]	0.718 [156]	0.732 [79]	0.758 (0.706, 0.810) [235 (range: (79, 365))]
msY _{16,MM} -Net	with	0.813 [117]	0.772 [175]	0.744 [307]	0.887 [252]	0.849 [213]	0.813 (0.763, 0.863) [213 (range: (117, 307))]
	without	0.831 [422]	0.873 [98]	0.770 [307]	0.909 [288]	0.867 [499]	0.850 (0.804, 0.896) [323 (range: (98, 499))]

tiny detail patch in its center (recall the relative sizes in figure 2), additional guidance, at least in this way, does not result in a consistent improvement. Still, the data in table 4 suggests that training with an additional classification loss may lead to more stable results (cf. splits 3 and 4). In addition, we have the impression that it speeds up and stabilizes convergence, though this effect is again not consistent.

6. Conclusions

Using the segmentation of hepatocellular carcinoma in hematoxylin-eosin stained whole-slide images of the liver as an example task, our results show that the extensive integration of widely different spatial scales, as a “mimicry” of how humans approach analogous tasks, offers significant and relevant improvements over a baseline U-Net as the de facto standard in histopathology image segmentation.

The study presents a family of models that can integrate context from multiple scales and at various levels. As an overarching effect, it shows that when fusing encoder paths from different scales, spatial alignment and preservation of spatial relationships is necessary. The presented multi-scale

merge block fulfils this requirement.

It goes without saying that future research is likely to optimize the models presented herein much further. As the detailed structure of encoder, decoder and possible skip connections are left entirely untouched, the proposed multi-scale architectures can seamlessly be adopted to various encoder-decoder models. In addition, we have shown how the proposed building blocks and the underlying intuition can be extended to arbitrary many arbitrarily sized spatial scales, whichever relevant for the particular organ and disease of interest. Moreover, additional and early merge connections may offer the possibility to make use of more complex relations between the different scales. As both we would expect both the relevant spatial scales as well as the complexity of the tasks to vary between applications, we envision that the proposed architectures open up a rich environment and search space also for neural architecture searches.

This study has important limitations: First of all, it is restricted to one particular task and organ and disease entity. It remains to future work to examine how these findings generalize to other tasks, organs and types of cancer or even other diseases. For this specific task, the study suggests that global context seems to be of particular im-

portance and more relevant than local context. In addition, we have seen no particular advantage of early or multiple merge connections which would allow for pronounced use of complex combined features. The latter two statements, however, may be explained by nature of the dataset under consideration and its specilties, namely hepatocellular carcinoma with their characteristic pseudocapsules which are very large-scale features. Therefore, testing of the models on tumor entities that are characterised by medium-scale context, such as glandular aberration in adenocarcinoma, may be of particular interest for further studies.

This study provides an example how a mimicry of how human experts approach a specific task can be used to develop specialized machine learning architectures. It advocates the integration of extensive multi-scale context into deep learning models for computational histopathology.

Acknowledgments

This study was partially supported by an unrestricted grant from Olympus Co Hamburg, Germany, and by the Forschungszentrum Medizintechnik Hamburg (02fmthh2017).

RS gratefully acknowledges funding by the Studienstiftung des deutschen Volkes and the Günther Elin Krempel foundation. TR receives study support for various projects from Olympus Co Hamburg, Germany, but declares that there is no conflict to disclose with regards to this project. RW received funding from Siemens Healthcare, Erlangen, Germany, but declares that there is no conflict to disclose regarding this project.

The authors would like to thank NVIDIA for the donation of a graphics card under the GPU Grant Program. In addition, the authors are grateful towards Hinnerk Stüben for his excellent technical support.

References

Badrinarayanan, V., Kendall, A., Cipolla, R., 2017. SegNet: A Deep Convolutional Encoder-Decoder Architecture for Image Segmentation. *IEEE Transactions on Pattern Analysis and Machine Intelligence* 39, 2481–2495. doi:10.1109/TPAMI.2016.2644615.

Bejnordi, B.E., Zuidhof, G., Balkenhol, M., Hermsen, M., Bult, P., van Ginneken, B., Karssemeijer, N., Litjens, G., van der Laak, J., 2017. Context-aware stacked convolutional neural networks for classification of breast carcinomas in whole-slide histopathology images. *Journal of Medical Imaging* 4, 1. doi:10.1117/1.JMI.4.4.044504.

Bouckaert, R.R., Frank, E., 2004. Evaluating the Replicability of Significance Tests for Comparing Learning Algorithms, in: Kanade, T., Kittler, J., Kleinberg, J.M., Matern, F., Mitchell, J.C., Nierstrasz, O., Pandu Rangan, C., Steffen, B., Sudan, M., Terzopoulos, D., Tygar, D., Vardi, M.Y., Weikum, G., Dai, H., Srikant, R., Zhang, C. (Eds.), *Advances in Knowledge Discovery and Data Mining*. Springer Berlin Heidelberg, Berlin, Heidelberg. volume 3056, pp. 3–12. doi:10.1007/978-3-540-24775-3_3. series Title: Lecture Notes in Computer Science.

Brierley, J.D., Gospodarowicz, M.K., Wittekind, C. (Eds.), . *TNM Classification of Malignant Tumours*, 8th Edition. UICC, Wiley-Blackwell.

Bulten, W., Bndi, P., Hoven, J., Loo, R.v.d., Lotz, J., Weiss, N., Laak, J.v.d., Ginneken, B.v., Hulsbergen-van de Kaa, C., Litjens, G., 2019. Epithelium segmentation using deep learning in H&E-stained prostate specimens with immunohistochemistry as reference standard. *Scientific Reports* 9. doi:10.1038/s41598-018-37257-4.

Campanella, G., Hanna, M.G., Geneslaw, L., Mirafior, A., Werneck Krauss Silva, V., Busam, K.J., Brogi, E., Reuter, V.E., Klimstra, D.S., Fuchs, T.J., 2019. Clinical-grade computational pathology using weakly supervised deep learning on whole slide images. *Nature Medicine* doi:10.1038/s41591-019-0508-1.

Chen, L.C., Papandreou, G., Kokkinos, I., Murphy, K., Yuille, A.L., 2017a. DeepLab: Semantic Image Segmentation with Deep Convolutional Nets, Atrous Convolution, and Fully Connected CRFs. arXiv:1606.00915 [cs] .

Chen, L.C., Papandreou, G., Schroff, F., Adam, H., 2017b. Rethinking Atrous Convolution for Semantic Image Segmentation. arXiv:1706.05587 [cs] .

Choi, J., Lee, K., Jeong, W.K., Chun, S.Y., Park, P., . Paip 2019 Challenge Dataset. URL: <https://paip2019.grand-challenge.org/Dataset/>.

Epstein, J.I., Egevad, L., Srigley, J.R., Humphrey, P.A., 2016. The 2014 International Society of Urological Pathology (ISUP) Consensus Conference on Gleason Grading of Prostatic Carcinoma. *Am J Surg Pathol* 40, 9.

He, K., Zhang, X., Ren, S., Sun, J., 2015. Deep Residual Learning for Image Recognition. arXiv:1512.03385 [cs] .

Isensee, F., Petersen, J., Klein, A., Zimmerer, D., Jaeger, P.F., Kohl, S., Wasserthal, J., Koehler, G., Norajitra, T., Wirkert, S., Maier-Hein, K.H., 2018. nnU-Net: Self-adapting Framework for U-Net-Based Medical Image Segmentation. arXiv:1809.10486 [cs] 00040 arXiv: 1809.10486.

Isensee, F., Petersen, J., Kohl, S.A.A., Jger, P.F., Maier-Hein, K.H., 2019. nnU-Net: Breaking the Spell on Successful Medical Image Segmentation. arXiv:1904.08128 [cs] .

Kamnitsas, K., Ledig, C., Newcombe, V.F., Simpson, J.P., Kane, A.D., Menon, D.K., Rueckert, D., Glocker, B., 2017. Efficient multi-scale 3d CNN with fully connected CRF for accurate brain lesion segmentation. *Medical Image Analysis* 36, 61–78. doi:10.1016/j.media.2016.10.004.

Kickingreder, P., Isensee, F., Tursunova, I., Petersen, J., Neuberger, U., Bonekamp, D., Brugnara, G., Schell, M., Kessler, T., Foltyn, M., Harting, I., Sahm, F., Prager, M., Nowosielski, M., Wick, A., Nolden, M., Radbruch, A., Debus, J., Schlemmer, H.P., Heiland, S., Platten, M., von Deimling, A., van den Bent, M.J., Gorlia, T., Wick, W., Bendszus, M., Maier-Hein, K.H., 2019. Automated quantitative tumour response assessment of MRI in neuro-

- oncology with artificial neural networks: a multicentre, retrospective study. *The Lancet Oncology* 20, 728–740. doi:10.1016/S1470-2045(19)30098-1. 00008.
- Kingma, D.P., Ba, J., 2014. Adam: A method for stochastic optimization. arXiv preprint arXiv:1412.6980 .
- Li, J., Sarma, K.V., Ho, K.C., Gertych, A., Knudsen, B.S., Arnold, C.W., 2017. A Multi-scale U-Net for Semantic Segmentation of Histological Images from Radical Prostatectomies. *AMIA Annu Symp Proc.* , 1140–1148.
- Li, S., Tso, G.K.F., 2019. Bottleneck Supervised U-Net for Pixel-wise Liver and Tumor Segmentation. arXiv:1810.10331 [cs] .
- Li, X., Chen, H., Qi, X., Dou, Q., Fu, C.W., Heng, P.A., 2018. H-DenseUNet: Hybrid Densely Connected UNet for Liver and Tumor Segmentation from CT Volumes. arXiv:1709.07330 [cs] .
- Litjens, G., Kooi, T., Bejnordi, B.E., Setio, A.A.A., Ciompi, F., Ghafoorian, M., van der Laak, J.A.W.M., van Ginneken, B., Snchez, C.I., 2017. A survey on deep learning in medical image analysis. *Medical Image Analysis* 42, 60–88. doi:10.1016/j.media.2017.07.005.
- Liu, W., Rabinovich, A., Berg, A.C., 2015. ParseNet: Looking Wider to See Better. arXiv:1506.04579 [cs] .
- Liu, Y., Gadepalli, K., Norouzi, M., Dahl, G.E., Kohlberger, T., Boyko, A., Venugopalan, S., Timofeev, A., Nelson, P.Q., Corrado, G.S., Hipp, J.D., Peng, L., Stumpe, M.C., . Detecting Cancer Metastases on Gigapixel Pathology Images. arXiv:1703.02442 , 13.
- Long, J., Shelhamer, E., Darrell, T., 2015. Fully Convolutional Networks for Semantic Segmentation. *Proceedings of the IEEE Conference on Computer Vision and Pattern Recognition* , 3431–3440.
- Mehta, S., Mercan, E., Bartlett, J., Weaver, D., Elmore, J.G., Shapiro, L., 2018. Y-Net: Joint Segmentation and Classification for Diagnosis of Breast Biopsy Images, in: Frangi, A.F., Schnabel, J.A., Davatzikos, C., Alberola-Lpez, C., Fichtinger, G. (Eds.), *Medical Image Computing and Computer Assisted Intervention MICCAI 2018*. Springer International Publishing, Cham. volume 11071, pp. 893–901. doi:10.1007/978-3-030-00934-2_99.
- Nadeau, C., Bengio, Y., 2000. Inference for the Generalization Error , 307–31300814.
- Oktay, O., Schlemper, J., Folgoc, L.L., Lee, M., Heinrich, M., Misawa, K., Mori, K., McDonagh, S., Hammerla, N.Y., Kainz, B., Glocker, B., Rueckert, D., 2018. Attention U-Net: Learning Where to Look for the Pancreas.
- Paszke, A., Gross, S., Chintala, S., Chanan, G., Yang, E., DeVito, Z., Lin, Z., Desmaison, A., Antiga, L., Lerer, A., 2017. Automatic differentiation in pytorch .
- R Core Team, 2013. R: A Language and Environment for Statistical Computing. R Foundation for Statistical Computing, Vienna, Austria. URL: <http://www.R-project.org/>.
- Reinhard, E., Ashikhmin, M., Gooch, B., Shirley, P., 2001. Color Transfer between Images. *IEEE Computer Graphics and Applications* , 802092.
- Ronneberger, O., Fischer, P., Brox, T., 2015. U-Net: Convolutional Networks for Biomedical Image Segmentation. *Medical Image Computing and Computer-Assisted Intervention MICCAI 2015* 9351, 234–241.
- Russakovsky, O., Deng, J., Su, H., Krause, J., Satheesh, S., Ma, S., Huang, Z., Karpathy, A., Khosla, A., Bernstein, M., Berg, A.C., Fei-Fei, L., 2015. ImageNet Large Scale Visual Recognition Challenge. *International Journal of Computer Vision* 115, 211–252. doi:10.1007/s11263-015-0816-y.
- Schmitz, R., Krause, J., Krech, T., Rsch, T., 2018. Virtual Endoscopy Based on 3-Dimensional Reconstruction of Histopathology Features of Endoscopic Resection Specimens. *Gastroenterology* 154, 1234–1236.e4. doi:10.1053/j.gastro.2017.11.291.
- Segovia-Miranda, F., Morales-Navarrete, H., Kcken, M., Moser, V., Seifert, S., Repnik, U., Rost, F., Brosch, M., Hendricks, A., Hinz, S., Rcken, C., Ltjohann, D., Kalaidzidis, Y., Schafmayer, C., Brusch, L., Hampe, J., Zerial, M., 2019. Three-dimensional spatially resolved geometrical and functional models of human liver tissue reveal new aspects of NAFLD progression. *Nature Medicine* 25, 1885–1893. doi:10.1038/s41591-019-0660-7. 00001.
- Vu, Q.D., Kwak, J.T., 2019. A Dense Multi-Path Decoder for Tissue Segmentation in Histopathology Images. *Computer Methods and Programs in Biomedicine* doi:10.1016/j.cmpb.2019.03.007.
- Wang, S., Zhu, Y., Yu, L., Chen, H., Lin, H., Wan, X., Fan, X., Heng, P.A., 2019. RMDL: Recalibrated Multi-instance Deep Learning for Whole Slide Gastric Image Classification. *Medical Image Analysis* , 101549doi:10.1016/j.media.2019.101549.
- Zhang, H., Dana, K., Shi, J., Zhang, Z., Wang, X., Tyagi, A., Agrawal, A., 2018. Context Encoding for Semantic Segmentation. arXiv:1803.08904 [cs] .
- Zhou, Y., Sun, X., Zha, Z.J., Zeng, W., 2019. Context-Reinforced Semantic Segmentation. *The IEEE Conference on Computer Vision and Pattern Recognition (CVPR)* , 4046–4055.
- Zink, D., Fischer, A.H., Nickerson, J.A., 2004. Nuclear structure in cancer cells. *Nature Reviews Cancer* 4, 677–687. doi:10.1038/nrc1430.

Supplementary Materials to: Multi-scale fully convolutional neural networks for histopathology image segmentation: from nuclear aberrations to the global tissue architecture

Rüdiger Schmitz*, Frederic Madesta, Maximilian Nielsen, Jenny Krause, René Werner**, Thomas Rösch**

S1. Base model architecture

A detailed view on our baseline model is provided through figure S1.

S2. Baseline model results

As described in section 4 of the main article, the experiments are repeated three times for the baseline model. The detailed results for each individual repetition are given in table S1.

S3. Class-specific Jaccard indices at convergence

Supplemental to what has been reported in section 5.1, the tables S2 and S3 show the class-specific validation Jaccard indices for the whole and the viable tumor area, respectively.

S4. Maximum Jaccard indices

Table S4 reports the maximum class-averaged Jaccard indices achieved by the individual models

and splits at any validation step throughout the training process, i.e. irrespective of whether convergence is reached or not. Whilst the results qualitatively resemble what has been discussed in section 5.1, it is interesting to note the Jaccard indices at convergence are notably smaller than their maximum values in some cases. This points to the fact that for intersection over union measures, such as the Jaccard index, cross entropy loss functions are not optimal Berman et al. (2018). There exist optimized loss functions as, for instance, the Lovász-Hinge loss described therein. In this study, aiming at a as much common setup as possible not only for the baseline model itself, the much more widely used cross entropy loss was used nevertheless (cf. section 2.3).

Supplementary References

Berman, M., Triki, A. R., and Blaschko, M. B. (2018). The lovasz-Softmax loss: A tractable surrogate for the optimization of the intersection-over-union measure in neural networks. *arXiv:1705.08790 [cs]*.

*Corresponding author: r.schmitz@uke.de

**Equal contribution.

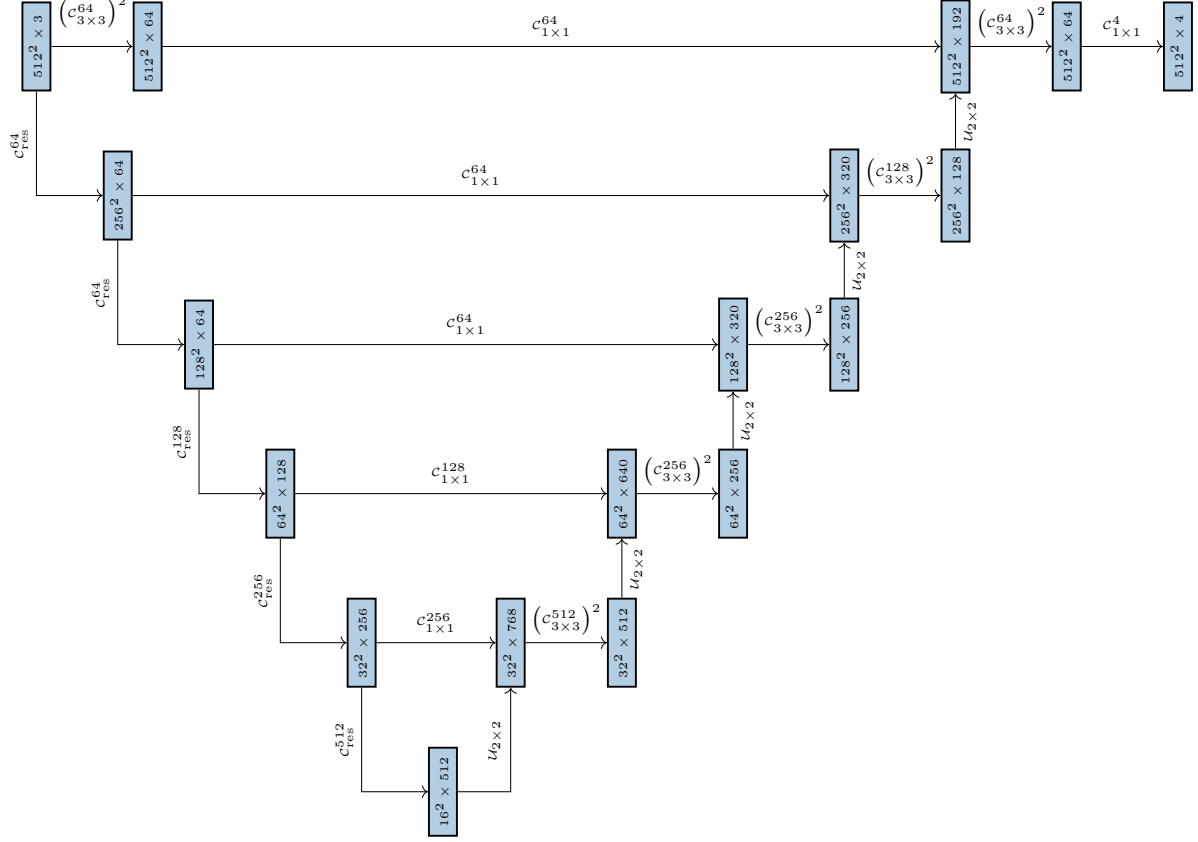


Figure S1: ResNet18-based U-Net architecture (baseline model). For each block the spatial image shape as well as the number of channels are given. Here, $\mathcal{C}_{m \times n}^{f_i, f_o}$ denotes a single $m \times n$ convolution with f_i input and f_o output feature maps, followed by ReLU activation. $(\mathcal{C}_{m \times n}^f)^l$ shall represent l consecutive $m \times n$ convolutions with f output maps, each followed by a ReLU activation function. For the encoding part, the blocks $(\mathcal{C}_{\text{res}}^f)$ of a ResNet18 are used where f denotes number of the respective output feature maps. Each individual block introduces a spatial downscaling by a factor of 2, either through max pooling or strided convolutions. The decoder uses $m \times n$ bilinear upsampling ($\mathcal{U}_{m \times n}$) to enlarge the spacial dimensions.

Table S1: Class-average of the validation Jaccard index for whole and viable tumor at convergence of the validation loss for the baseline model in three independent training runs.

	CV folds				
	0	1	2	3	4
Run 0	0.759	0.690	0.607	0.700	0.689
Run 1	0.748	0.692	0.674	0.702	0.690
Run 2	0.789	0.711	0.636	0.710	0.648

Table S4: Selected multi-scale multi-encoder setups versus the baseline U-Net. The numbers show the class-average validation Jaccard index throughout the training process of the given CV split (whether converged, as judged by the validation loss, or not). A \star again denotes statistical significance at the level of 0.05. For the other comparisons described in section 5.1, the null hypothesis cannot be rejected at 0.05. The bold markings and the architecture nomenclature are as in the previous tables.

Arch.	Scales	CV folds					Mean (95% CI)				
		0	1	2	3	4					
U-Net	1	0.776	0.735	0.663	0.711	0.703	0.718 (0.681, 0.754)				
msY-Net	1, 4	0.883	0.752	0.687	0.755	0.745	0.764 (0.701, 0.827)		\star		
	1, 16	0.837	0.860	0.791	0.868	0.876	0.846 (0.816, 0.876)			\star	
msUI-Net	1, 4	0.788	0.798	0.767	0.852	0.881	0.817 (0.776, 0.859)				
	1, 16	0.854	0.825	0.788	0.902	0.878	0.849 (0.810, 0.888)				\star
msYI-Net	1, 4, 16	0.838	0.867	0.807	0.915	0.906	0.867 (0.827, 0.906)				
msY ² -Net	1, 4, 16	0.861	0.830	0.779	0.901	0.842	0.843 (0.803, 0.882)				